L_1 Adaptive Control of a Dual-Rotor Tail-Sitter Unmanned Aerial Vehicle With Input Constraints During Hover Flight

JINGYANG ZHONG[1], BIFENG SONG[1], YUBIN LI[2], AND JIANLIN XUAN[3]

[1]School of Aeronautics, Northwestern Polytechnical University, Xi'an 710072, China
[2]Research and Development Institute, Northwestern Polytechnical University, Shenzhen 518057, China
[3]Yangtze River Delta Research Institute, Northwestern Polytechnical University, Taicang 215400, China

Corresponding author: Jingyang Zhong (zjynwpu@mail.nwpu.edu.cn)

ABSTRACT The input constraints of control surfaces may lead to saturations, which could limit the achievable performance or even cause instability of vertical take-off and landing (VTOL) tail-sitter unmanned aerial vehicle (UAV). To improve flight safety and attitude tracking performance, a novel L_1 adaptive control architecture for attitude tracking of a tail sitter subjected to input constraints is proposed in this study. The imprecise mathematical model, low weight, and small size all present different challenges when designing a control system. In this work, a feedforward compensator is first used to narrow down the uncertain bounds with the consideration of finite accuracy from prior knowledge. Second, according to the linearized model, a baseline controller is designed to offer basic performance for a nominal system without uncertainty. Finally, the L_1 adaptive controller is developed to compensate for unmatched uncertainties based on the control system developed before. The stability and performance bounds of the closed-loop system are analyzed to illustrate the impact of input constraints. The numerical simulations and flight tests are carried out to verify the improved attitude tracking performance when input saturation exists.

INDEX TERMS Tail-sitter, L_1 adaptive control, hover attitude control, input constrains.

I. INTRODUCTION

Small unmanned aerial vehicles (UAVs) have a worldwide impact both in military and civilian use and the main benefits are extending and complementing human performance [1]. Vertical take-off and landing (VTOL) UAVs combine the advantages of both fixed-wing and rotary-wing aircraft which make these UAVs more applicable for carrying out a task [2]. These UAVs can take off and land quickly in a confined area and have the ability to both hover and cruise to reach the mission point quickly or perform surveillance jobs [3].

Compared to other VTOL UAVs in the literature, such as tilting-rotor, tilting-wing, thrust-vectoring and quadrotor hybrid vehicles, the major advantage of a tail-sitter is its unnecessity for a transition mechanism that improves the reliability of the system and saves weight [4], [5]. A common configuration of a tail-sitter is the dual-rotor layout, which uses propellers combined with two control surfaces submerged within the slipstream generated from propellers to produce control moments. Many researchers and organizations have focused on related studies of dual rotor tail-sitter aerial vehicles. Stone *et al.* developed a dual-rotor tail-sitter named "T-Wing" [6], [7], and aerodynamics, aircraft design and control have been studied since 1996. Forshaw *et al.* developed a twin helicopter rotor tail sitter called "QinetiQ's Eye-On" in 2011 [8], [9]. Bilodeau and Wong developed a TS-MAV testbed in 2010 [10]. Verling *et al.* developed a tail sitter named "Pacflyer S100" in 2016 [11] and the focus was on full attitude control. Likewise, a dual-rotor tail-sitter aerial vehicle is also established as our research object.

The imprecise aerodynamic knowledge, moment of inertia and unknown disturbances present significant challenges to a small tail-sitter aerial vehicle from a control design perspective. The size of the control surface should also be designed appropriately to take into account both the hover and forward flight stages. Furthermore, the situation is also complicated

---

The associate editor coordinating the review of this manuscript and approving it for publication was Rosario Pecora.

by the finite effect of control surfaces during the hover stage because the time-varying propeller slipstreams [12] are the only contributions to dynamic pressure for generating pitch and yaw control moments. The variations in dynamics and disturbances make it a reasonable choice to implement model reference adaptive control (MRAC) architecture, which can identify the uncertainty parameters online [13]. However, the performance of MRAC is limited by the adaptive gains while large adaptive gains may lower the robustness of the system [14], [15]. Based on this drawback of MRAC architecture, Cao and Hovakimyan first proposed L_1 adaptive control theory in 2006 [16], [17]. The key feature of the L_1 adaptive control architecture is guaranteed robustness in the presence of fast adaptation, which leads to uniform performance bounds both in transient and steady-state operation [18]. With L_1 adaptive control architectures, large learning gains appear to be beneficial both for performance and robustness, while the tradeoff between the two is resolved by selecting the underlying filter structure and the speed of adaptation is limited only by the available hardware [19]–[22].

In recent years, the L_1 adaptive control architecture has attracted the interest of many researchers in UAV control design. Monte *et al.* designed an adaptive backstepping controller for the position trajectory tracking of a quadrotor [23]. The simulation results considered the L_1 adaptive control a promising solution to handle various parameter uncertainties. Gregory *et al.* presented the results of a flight test of the L_1 adaptive control architecture designed to directly compensate for significant uncertain cross-coupling for a subscale turbine powered Generic Transport Model that is an integral part of the Airborne Subscale Transport Aircraft Research system at the NASA Langley Research Center [24]. The results showed that the L_1 flight control law provides predictable behavior both in the neighborhood of the design point and in other operating points of the flight envelope. Banerjee *et al.* developed an L_1 adaptive control augmentation for the longitudinal dynamics of a hypersonic glider and presented a comparative study of the performance and robustness of two types of controller: the pole placement controller and L_1 augmented controller [25]. Capello *et al.* developed an L_1 adaptive algorithm as the attitude loop controller for a small flying wing UAV [26]. That paper demonstrated that, if an L_1 algorithm is considered for the attitude loop, no retuning or gain scheduling is required, even if a nonlinear complete system is considered.

Despite many works studying UAVs with L_1 adaptive control architecture, few studies have applied this architecture to tail-sitters. Furthermore, previous studies with L_1 adaptive control architecture did not explicitly consider the input constraints. Due to the finite deflection of the control surface for a tail-sitter UAV during the hover stage, the input-constraint induced saturation may limit the achievable performance or even cause instability. Therefore, it might be important to consider the input constraints when designing a control system. To the best of our knowledge, only Li *et al.* in his studies explicitly considered the input

saturation [27]–[29]. The way he considered that was by adding a saturation function in the state predictor, and simulation was conducted for verification but not applied to a real object. Furthermore, Vanness *et al.* proposed a proportional adaptation law for the L_1 adaptive control architecture; the reduction in the required computational resources made this approach more capable for engineering implementation, while only simulation results were shown to illustrate the performance of the controller and no input constraints were considered in his studies [30].

Inspired by the thoughts from [31] and based on the analysis for the source of input saturation in the L_1 adaptive control architecture, we propose a new way to consider input constraints during controller design for the proportional adaptation law of L_1 adaptive control architectures. The main contribution of this work is that we propose a novel L_1 adaptive control architecture for attitude tracking of a VTOL tail-sitter UAV subjected to input constraints. The stability and performance bounds of the closed-loop system are analyzed to illustrate the impact of input constraints. The simulation results show that the performance of the closed-loop system can be improved by the method we propose in this study when control surface saturation exists. In addition, to the best of our knowledge, no previous study has tried to use the L_1 adaptive architecture of proportional adaptation law in real flight tests, not to mention realizing the improved method we propose in this study. Therefore, flight tests are also used to demonstrate the benefit of the proposed control methodology.

The rest of this paper is organized as follows. Section II presents the system description and kinematics and dynamics model of the dual rotor tail sitter in this study and formulate the design problem with input constraints. Section III proposes the detailed control system design process and analyses the stability and performance bounds of a closed-loop system with consideration of input constraints. In Section IV, simulation results verify the benefit of the proposed methodology and flight test results are given in Section V. Finally, we draw some concluding remarks in Section VI.

II. TAIL-SITTER UAV SYSTEMS MODELING
In this section, the detailed configuration of the tail-sitter UAV is described and the design problem with input constraints is formulated.

A. SYSTEM DESCRIPTION
A flying-wing tail-sitter UAV is established as the research objective in this work as shown in Figure 1. The UAV is modified from a commercial platform called "TBS Caipirinha" [32]. Two 3D-printed motor mounts are attached on each wing side such that the motor axis will be roughly going through the center of the elevons and the horizontal distance between the two motor mounts are 52cm [33]. Two control surfaces are attached to the back side of the wing using fiber tape. In hover flight state, the differential thrust of two propellers are used to provide rolling moment. The symmetry and asymmetry deflection of control surfaces are for pitching
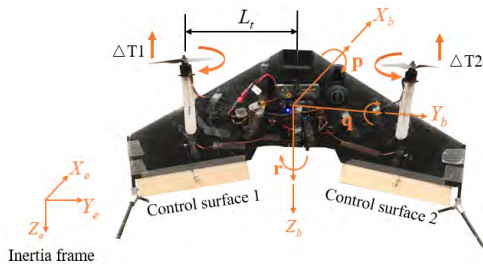
FIGURE 1. The prototype of the tail sitter.

TABLE 1. Tail-sitter parameters.

Parameter	Description	Value
m	mass	0.81 kg
c	reference chord	0.253 m
b	reference span	0.8774 m
δe	control surface deflection	$\pm 20\,^\circ$
J	inertia matrix	[0.025 0.007 0.022] kg·m²
C_{sc}	control surface chord	0.05 m
C_{ss}	control surface span	0.3 m
T	motor thrust	0.625 kg

TABLE 2. Dimensionless aerodynamic coefficients.

Parameter	Description	Value
C_{mq}	pitch damping coefficient	-1.01
C_{lp}	roll damping coefficient	-0.016
C_{nr}	yaw damping coefficient	-0.327
$C_{l\beta}$	lateral stability derivative	-0.0001
$C_{m\delta e}$	pitch control derivative	-0.2857
C_{l0}	rolling moment coefficient at zero angle of attack	-0.00005
C_{lr}	roll cross derivative	0.026
$C_{m\alpha}$	pitch moment coefficient curve slope	-0.1085
C_{n0}	yawing moment coefficient at zero angle of attack	-0.00003
$C_{n\beta}$	directional stability derivative	-0.00003
C_{np}	yaw cross derivative	0.024
C_{m0}	pitching moment coefficient at zero angle of attack	-0.036
$C_{n\delta e}$	yaw control derivative	0.1562

and yawing control and slipstream generated by propellers has a critical impact on the efficiency of the control surfaces. where L_t denotes horizontal distance between the motor and center of gravity of the aircraft. $\Delta T1$ and $\Delta T2$ represent the thrust variations of left motor and right motor, respectively.

The main system parameters and the dimensionless aerodynamic parameters of the UAV are listed in Table 1 and Table 2 respectively according to previous studies [34].

B. DYNAMIC MODEL

The Euler angle description is used as the rotation of a body-fixed coordinate frame (X_b, Y_b, Z_b) about a flat Earth reference frame (X_e, Y_e, Z_e). The origin of the body-fixed coordinate frame is the center of gravity of the body, and the body is assumed to be rigid. The flat Earth reference frame is considered inertial. The relationship between the angular

position with the definition of $\Omega = [\varphi, \theta, \psi]$ and the angular rates with the definition of $\omega = [p, q, r]$ can be described as follows

$$\dot{\Omega} = R\omega \qquad (1)$$

where R is defined as

$$R = \begin{bmatrix} 1 & \sin\phi\tan\theta & \cos\phi\tan\theta \\ 0 & \cos\phi & -\sin\phi \\ 0 & \sin\phi\sec\theta & \cos\phi\sec\theta \end{bmatrix}$$

The dynamic equations of motion for the UAV are described by

$$\dot{\omega} = -B(\omega \times J\omega) + BM \qquad (2)$$

where $B = J^{-1}$ denotes the inverse of the inertia matrix of the vehicle and M is the total moment acting on the UAV; M can be further divided as

$$M = M_{aero} + M_{un} + u \qquad (3)$$

$$u(t) = u_{max} sat\left(\frac{u_c(t)}{u_{max}}\right) = \begin{cases} u_c(t), & |u_c(t)| \le u_{max} \\ u_{max}\,\text{sgn}(u_c(t)), & |u_c(t)| > u_{max} \end{cases}$$
$$(4)$$

where M_{aero} denotes the aerodynamic moment acting on the wing, M_{un} denotes the aerodynamic parameter uncertainty and the disturbance moment, u denotes the actual control moment generated by the rotating propellers and control surfaces, u_c denotes the desired control moment computed by the controller, u_{max} denotes the largest moment that the propellers and control surfaces could achieve and sgn (·) is the sign function.

$$M_{aero}$$
$$= \begin{bmatrix} l_{aero} \\ m_{aero} \\ n_{aero} \end{bmatrix}$$
$$= \begin{bmatrix} 0.5\rho V^2 Sb\left(C_{l0} + C_{l\beta}\beta + C_{lp}\dfrac{b}{2V}p + C_{lr}\dfrac{b}{2V}r\right) \\ 0.5\rho V^2 Sc\left(C_{m0} + C_{m\alpha}\alpha + C_{mq}\dfrac{c}{2V}q\right) \\ 0.5\rho V^2 Sb\left(C_{n0} + C_{n\beta}\beta + C_{np}\dfrac{b}{2V}p + C_{nr}\dfrac{b}{2V}r\right) \end{bmatrix}$$
$$(5)$$

$$u = \begin{bmatrix} l_c \\ m_c \\ n_c \end{bmatrix} = \begin{bmatrix} \Delta T L_t \\ C_{m\delta_e}\delta_{e(pitch)} \\ C_{n\delta_e}\delta_{e(yaw)} \end{bmatrix} \qquad (6)$$

where l_{aero}, m_{aero}, and n_{aero} are aerodynamic moments of the wing in the roll, pitch and yaw directions, respectively; α is the angle of attack; β is the angle of sideslip; and l_c, m_c, and n_c are moments generated by the actuators.

Note that due to the physical nature, there is no uncertainties in (1), and the dynamics of ω in (2) and (3) may be represented as follows:

$$\dot{\omega} = B_m u + f_0(t, \omega) \qquad (7)$$
$$f_0(t, \omega) = -B(\omega \times J\omega) + \Delta B(M_{aero} + M_{un} + u)$$
$$+ B_m(M_{aero} + M_{un}) \qquad (8)$$
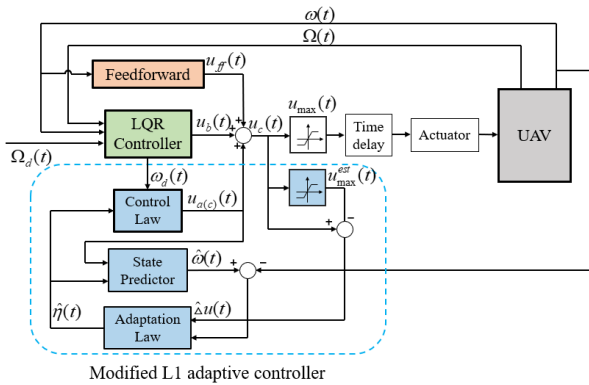
Modified L1 adaptive controller

FIGURE 2. Control system architecture.

where $B = B_m + \Delta B$, B_m denotes the best estimation of the inverse of the inertia matrix and ΔB denotes the estimation error.

III. CONTROL DESIGN WITH INPUT CONSTRAINTS
The control methodologies that were employed to carry out this study are presented in this section.

The feedforward compensator makes best use of known aerodynamic and rigid body dynamic characteristics but also takes into consideration the finite precision of these parameters. The baseline controller is implemented with the help of the linear quadratic regulator technique. Then, an L_1 adaptive controller with consideration of input constraints is developed to augment for the uncertainties in (7). Let $u_c(t)$ be defined as

$$u_c(t) = u_{ff}(t) + u_b(t) + u_{a(c)}(t) \tag{9}$$

where $u_{ff}(t)$, $u_b(t)$, and $u_{a(c)}(t)$ denote the feedforward compensator, baseline controller and L_1 adaptive controller, respectively as shown in Figure 2.

IV. FEEDFORWARD COMPENSATOR
The inertial coupling terms $\omega \times J\omega$ in (2) are deduced from Newton-Euler equations and are used widely in aircraft modeling, so these terms are treated as high confidence terms. Additionally, in view of the finite precision of the aerodynamic parameters, only dominating items are used. Therefore, the feedforward compensator is defined as follows

$$u_{ff}(t) = \alpha_1 \omega(t) \times J\omega(t)$$
$$- 0.5\rho V(t)^2 S \begin{pmatrix} b\left(\alpha_2 C_{l0} + \alpha_3 C_{lp}\dfrac{b}{2V(t)}p(t)\right) \\ c\left(\alpha_2 C_{m0} + \alpha_3 C_{mq}\dfrac{c}{2V(t)}q(t)\right) \\ b\left(\alpha_2 C_{n0} + \alpha_3 C_{nr}\dfrac{b}{2V(t)}r(t)\right) \end{pmatrix} \tag{10}$$

where $\alpha_1 \in [0, 1]$, $\alpha_2 \in [0, 1]$ and $\alpha_3 \in [0, 1]$ are weight coefficients defining how much the inertia moments and aerodynamic moments are fed forward into the control system.

The choices of α_2 and α_3 should be given particular attention to avoid overcompensation because of the finite precision of the aerodynamic parameters.

The dynamics of ω can then be written as

$$\dot{\omega}(t) = B_m (u_b(t) + u_a(t)) + f_1(t, \omega(t)) \tag{11}$$
$$f_1(t, \omega(t)) = -B(\omega(t) \times J\omega(t)) + B_m(M_{aero}(t) + M_{un}(t))$$
$$+ \Delta B(M_{aero}(t) + M_{un}(t) + u(t)) + B_m u_{ff}(t) \tag{12}$$

The feedforward compensator can narrow down the bounds of uncertainties $f_0(t, \omega(t))$ under appropriate choice of the weight coefficients.

A. BASELINE CONTROLLER
Linear quadratic regulator (LQR) control is a very attractive control approach because it easily handles multiple actuators and complex system dynamics. Furthermore, this approach can offer large stability margins to errors [35]. Therefore, an optimal LQR method is developed as a baseline controller for this system.

A linear model is necessary to design the LQR controller. The kinematics equation (1) and dynamic equation (11) near the hover equilibrium point can be linearized as in state-space form without considering uncertainties as follows:

$$\dot{x}(t) = A_{lqr}x(t) + B_{lqr}u_b(t) \tag{13}$$

where $x = [\Omega, \omega]$ is the state vector, and $A_{lqr} = [0_{3\times3}, I_{3\times3}; 0_{3\times3}, 0_{3\times3}]$ and $B_{lqr} = [0_{3\times3}; B_{m3\times3}]$ are responding Jacobian matrices.

The Euler angle error is defined as

$$\Omega_e(t) = \Omega(t) - \Omega_d(t) \tag{14}$$

where Ω_d denotes the desired tracking Euler angle. In flight control, Ω_d is often assumed to be a constant, which could represent the stick force coming from a pilot or the guidance command coming from the outer-loop steering algorithms. Even though these command signals are not actually constant, it has been proved very effective in most applications [13], which means that $\dot{\Omega}_d = 0_{3\times1}$ is reasonable. By defining a new state $x_{new} = [\Omega_e, \omega]$, (13) can be rewritten as

$$\dot{x}_{new}(t) = A_{lqr}x_{new}(t) + B_{lqr}u_b(t) \tag{15}$$

The LQR controller can automatically select optimal gains according to the following quadratic cost function.

$$J = \int_0^\infty \left[x_{new}(t)^T Q x_{new}(t) + u_b(t)^T R u_b(t)\right]dt \tag{16}$$

where the matrices Q and R are a 6×6 diagonal matrix and a 3×3 diagonal matrix, respectively.

The solution is a linear state feedback of the following form:

$$u_b(t) = -Kx_{new}(t) = -K_1\Omega_e(t) - K_2\omega(t) \tag{17}$$

where $K = R^{-1}B_{lqr}^T P$, P is found by solving the algebraic Riccati equation (ARE) for the positive semidefinite symmetric solution P as follows:

$$A_{lqr}^T P + PA_{lqr} + Q - PB_{lqr}R^{-1}B_{lqr}^T P = 0 \quad (18)$$

By substituting (17) into (15), the linearized dynamic equation of ω can be obtained as

$$\dot{\omega}(t) = A_m\omega(t) - B_mK_1\Omega_e(t) \quad (19)$$

where $A_m = -B_mK_2$ is the Hurwitz matrix; in addition, (19) can be rewritten as in the following form:

$$\dot{\omega}(t) = A_m\omega(t) + B_m\frac{-1}{A_m^{-1}B_m}\left(A_m^{-1}B_mK_1\Omega_e(t)\right) \quad (20)$$

then we have $\omega_d(t) = A_m^{-1}B_mK_1\Omega_e(t)$, which defines the desired angular rates that the L_1 adaptive controller should follow.

B. L_1 ADAPTIVE CONTROL DESIGN WITH INPUT CONSTRAINTS

Assumption 1: The feedforward compensator and baseline controller would not saturate the system, then $u_m(t) = u_b(t) + u_{ff}(t)$ is used for simplification which means $||u_m(t)|| < u_{max}$.

From (11), (17) with input constraints, the angular rates dynamics can be written as

$$\dot{\omega}(t) = A_m\omega(t) + B_m\left(u_a(t) - K_1\Omega_e(t)\right) + f_1(t, \omega(t)) \quad (21)$$

Letting $f(t, \omega(t)) = f_1(t, \omega(t)) - B_mK_1\Omega_e(t)$, (21) can be rewritten as

$$\dot{\omega}(t) = A_m\omega(t) + B_mu_a(t) + f(t, \omega(t)) \quad (22)$$

$$u_a(t) = \begin{cases} u_{a(c)}(t), & \left|u_{a(c)}(t) + u_m(t)\right| \leq u_{max} \\ u_{max}\,\mathrm{sgn}\left(u_{a(c)}(t) + u_m(t)\right) - u_m(t), & \\ & \left|u_{a(c)}(t) + u_m(t)\right| > u_{max} \end{cases} \quad (23)$$

where $u_{a(c)}(t)$ is the command control input calculated by L_1 adaptive controller and u_{max} is the same as in (4).

The control objective is to design an adaptive controller to ensure that the angular rates $\omega(t)$ would follow the desired angular rates $\omega_d(t)$ generated by the baseline controller with quantifiable bounds in both transient and steady states subject to input constraints defined in (23).

Assumption 2 (Bound of $f(t, \omega(t))$): There exists $B_L > 0$, such that $||f(t, 0)||_\infty \leq B_L$.

Assumption 3 (Semiglobal Uniform Boundedness of Partial Derivatives): For arbitrary $\delta > 0$, $d_{f\omega}(\delta) > 0$ and $d_{ft}(\delta) > 0$ exist independent of time, such that for arbitrary $||\omega||_\infty \leq \delta$, the partial derivatives of $f(t, \omega(t))$ are piecewise-continuous and bounded as follows:

$$\left\|\frac{\partial f(t, \omega)}{\partial\omega}\right\|_1 \leq d_{f\omega}(\delta), \quad \left|\frac{\partial f(t, \omega)}{\partial t}\right| \leq d_{ft}(\delta)$$

From Assumption 3, we can conclude the following Assumption 4.

Assumption 4 (Semiglobal Lipschitz Condition): For arbitrary $\delta > 0$, positive K_δ exists, such that $||f(t, \omega_1) - f(t, \omega_2)||_\infty \leq K_\delta||\omega_1 - \omega_2||_\infty$ for all $||\omega||_\infty \leq \delta$, uniformly in t.

The L_1 adaptive controller presented in this paper, similar to all other L_1 architectures, comprises a state predictor, adaptation law and control law.

1) STATE PREDICTOR
We consider the following state predictor, which has a similar structure as (22):

$$\dot{\hat{\omega}}(t) = A_m\hat{\omega}(t) + B_mu_{a(c)}(t) + \hat{\eta}(t) \quad (24)$$

where $\hat{\omega}(t) \in R$ are the predictor states; $\hat{\eta}(t)$ is the adaptive estimates of $f(t, \omega(t))$; and $u_{a(c)}(t)$ is the command control input without constraints and is different from the input in (22).

2) ADAPTATION LAW
The adaptive estimates are governed by

$$\hat{\eta}(t) = -\Gamma\left(\tilde{\omega}(t) - \kappa\hat{\Delta}u(t)\right) \quad (25)$$

where $\Gamma \in R^+$ is the adaptation gain and it is limited by only the available hardware, that is, the CPU clock speed, $\kappa \in R^+$ defines how quickly we want the control inputs out of saturation, $\tilde{\omega}(t) = \hat{\omega}(t) - \omega(t)$ is the prediction error, $\Delta u(t)$ represents the control deficiency and is defined as

$$\begin{aligned} \Delta u(t) &= u_{a(c)}(t) - u_a(t) \\ &= \left(u_m(t) + u_{a(c)}(t)\right) - \left(u_m(t) + u_a(t)\right) \\ &= u_c(t) - u_{max}sat\left(\frac{u_c(t)}{u_{max}}\right) \end{aligned} \quad (26)$$

Considering that the real u_{max} may not be measured, u_{max}^{est} is used to replace u_{max} and is chosen as the estimation of the real u_{max}. Then, (26) can be replaced by

$$\hat{\Delta}u(t) = u_c(t) - u_{max}^{est}sat\left(\frac{u_c(t)}{u_{max}^{est}}\right) \quad (27)$$

3) CONTROL LAW
The control signal is generated as the output of the following system

$$u_{a(c)}(s) = -C(s)\left(\phi(s)\hat{\eta}(s) - k_g\omega_d(s)\right) \quad (28)$$

$$\varphi(s) \triangleq \frac{(sI - A_m)^{-1}}{(sI - A_m)^{-1}B_m} \quad (29)$$

where $C(s) = (I_{3\times3} + K_fD(s))^{-1}K_fD(s)$ and $D(s)$ represents a strictly proper transfer function, chosen to ensure that $C(s)$ has unit DC gain. The choice of $C(s)$ also needs to render $C(s)\varphi(s)(sI - A_m)$ stable and proper. $\hat{\eta}(s)$ and $\omega_d(s)$ are the Laplace transforms of $\hat{\eta}(t)$ and $\omega_d(t)$, respectively.

To streamline the subsequent analysis of stability and performance bounds, we need to introduce some notation.

Let

$$H(s) = (sI - A_m)^{-1} B_m \qquad (30)$$

$$H_0(s) = (sI - A_m)^{-1} \qquad (31)$$

$$G(s) = H(s)(1 - C(s))\varphi(s) \qquad (32)$$

4) REFERENCE SYSTEM

The key feature of the L_1 adaptive controller is that it only compensates the low-frequency content of the uncertainty and the benefit of this approach is that it allows for avoiding the undesirable behavior of the control signal and keeping the time-delay margin bounded away from zero. However, the L_1 adaptive controller does not behave similarly to the ideal system $\dot{\omega}_{ideal}(t) = A_m \omega_{ideal}(t) + B_m k_g \omega_d(t)$ and $k_g = -(A_m^{-1} B_m)^{-1}$ due to the limited bandwidth of the control channel enforce by $C(s)$. Instead, the closed-loop system is approximating the reference system. To derive the dynamics of the reference systems for L_1 adaptive controller, the system's uncertainties are assumed to be precisely known.

We consider the following closed-loop reference system, in which the control signal only attempts to compensate for the uncertainties within the bandwidth of the low-pass filter $C(s)$:

$$\dot{\omega}_{ref}(t) = A_m \omega_{ref}(t) + B_m u_{a\_ref}(t) + \eta_{ref}(t) \qquad (33)$$
$$\eta_{ref}(t) \triangleq f(t, \omega_{ref}(t))$$

$$u_{a(c)\_ref}(s) = -C(s)\left(\phi(s)\eta_{ref}(s) - k_g \omega_d\right) \qquad (34)$$

$$u_{a\_ref}(t) = \begin{cases} u_{a(c)\_ref}(t), & \left| u_{a(c)\_ref}(t) + u_m(t) \right| \le u_{max} \\ u_{max} sgn\left(u_{a(c)\_ref}(t) + u_m(t)\right) - u_m, \\ \qquad\qquad \left| u_{a(c)\_ref}(t) + u_m(t) \right| > u_{max} \end{cases} \qquad (35)$$

By denoting $\Delta u_{ref}(t) = u_{a(c)\_ref}(t) - u_{a\_ref}(t)$, and letting Δ_{u_ref} be the upper bound of $\Delta u_{ref}(t)$, then $||\Delta u_{ref}||_{L\infty} \le \Delta_{u\_ref}$.

Lemma 1: Consider the stability of an input-output model of dynamical systems, and refer to a system as $y = gj$, where g denotes the map from the input $j(t) \in R^m$ to the output $y(t) \in R^l$. Assume that $g(t) \in L_1$, i.e., $||g||_{L1} < \infty$. Then for arbitrary $j(t) \in L_\infty$, we have

$$\|y_\tau\|_{L\infty} \le \|g\|_{L_1} \|j_\tau\|_{L\infty} \qquad (36)$$

and $y(t) \in L_\infty$. The proof is given in [18].

Notice that the consequence of the lowpass filter in the control channel is that the stability of the reference system is not guaranteed a priori as it is for the ideal system. Therefore, the stability of the reference system should be proved and this would be given in Lemma 2.

Lemma 2: For the closed-loop reference system in (33-35), subject to the L_1-norm conditions

$$\|G(s)\|_{L_1} < \frac{\rho_r - \left\|H(s)C(s)k_g\right\|_{L_1} \|\omega_d\|_{L\infty}}{L_{\rho_r}\rho_r + B} \\ - \frac{\left\|H(s)\phi(s)\right\|_{L_1} \Delta_{u\_ref} + \rho_{in}}{L_{\rho_r}\rho_r + B} \qquad (37)$$

if

$$\|\omega_0\|_\infty \le \rho_0 \qquad (38)$$

then the following bounds hold:

$$\left\|\omega_{ref_\tau}\right\|_{L\infty} \le \rho_r \qquad (39)$$

$$\left\|u_{a(c)\_ref_\tau}\right\|_{L\infty} \le \rho_{ur} \qquad (40)$$

Proof: The proof is done by contradiction. From (33), it follows that

$$\dot{\omega}_{ref}(t) = A_m \omega_{ref}(t) + B_m u_{a\_ref}(t) + \eta_{ref}(t) \qquad (41)$$

$$\dot{\omega}_{ref}(t) = A_m \omega_{ref}(t) + B_m u_{a(c)\_ref}(t) + \eta_{ref}(t) - \Delta u_{ref}(t) \qquad (42)$$

$$\omega_{ref}(s) = G(s)\eta_{ref}(s) + H(s)C(s)k_g \omega_d(s) \\ + \omega_{in}(s) - H(s)\phi(s)\Delta u_{ref}(s) \qquad (43)$$

From Lemma 1, we have

$$\left\|\omega_{ref\tau}\right\|_{L\infty} \le \|G(s)\|_{L_1} \left\|\eta_{ref\tau}\right\|_{L\infty} + \left\|H(s)C(s)k_g\right\|_{L_1} \|\omega_d\|_{L\infty} \\ + \|\omega_{in}\|_{L\infty} + \|H(s)\phi(s)\|_{L_1} \left\|\Delta u_{ref}\right\|_{L\infty} \qquad (44)$$

$$\left\|\omega_{ref\tau}\right\|_{L\infty} \le \|G(s)\|_{L_1} \left\|\eta_{ref\tau}\right\|_{L\infty} + \left\|H(s)C(s)k_g\right\|_{L_1} \|\omega_d\|_{L\infty} \\ + \|\omega_{in}\|_{L\infty} + \|H(s)\phi(s)\|_{L_1} \Delta_{u\_ref} \qquad (45)$$

If (39) is not true, since $||\omega_{ref}(0)||_\infty = ||\omega_0||_\infty \le \rho_0 \le \rho_r$ and $\omega_{ref}(t)$ is continuous, then $\tau > 0$ exists such that

$$\left\|\omega_{ref}(t)\right\|_\infty < \rho_r, \quad \forall t \in [0, \tau) \qquad (46)$$

and

$$\left\|\omega_{ref}(\tau)\right\|_\infty = \rho_r \qquad (47)$$

which implies that

$$\left\|\omega_{ref}(\tau)\right\|_{L\infty} = \rho_r \qquad (48)$$

Let

$$L_\delta \triangleq \frac{\bar{\delta}(\delta)}{\delta} d_{f\omega}(\bar{\delta}(\delta)), \quad \bar{\delta}(\delta)\delta + \bar{\gamma}_1 \qquad (49)$$

where $d_{f\omega}(\cdot)$ was introduced in Assumption 3; we have $\rho_r < \bar{\rho}_r(\rho_r)$. Then, taking Assumption 2 and Assumption 3 into consideration, the equality in (48), together with the redefinition in (49), yields the following upper bound

$$\left\|\eta_{ref\tau}\right\|_{L\infty} \le L_{\rho_r}\rho_r + B_L \qquad (50)$$

By substituting this upper bound into (45) and noticing that $||(\cdot)_\tau||_{L\infty} \le ||\cdot||_{L\infty}$ for uniformly bounded signals, we obtain the following:

$$\left\|\omega_{ref\tau}\right\|_{L\infty} \le \|\omega_{in}\|_{L\infty} + \left\|H(s)C(s)k_g\right\|_{L_1} \|\omega_d\|_{L\infty} \\ + \|H(s)\phi(s)\|_{L_1} \Delta_{u\_ref} + \|G(s)\|_{L_1} \\ \times \left(L_{\rho_r}\rho_r + B_L\right) \qquad (51)$$

Then, the L_1-norm condition is used to solve for ρ_r to obtain the upper bound as follows:

$$\|G(s)\|_{L_1}\left(L_{\rho_r}\rho_r + B_L\right) + \left\|H(s)C(s)k_g\right\|_{L_1} \|\omega_d\|_{L\infty} \\ + \|\omega_{in}\|_{L\infty} + \|H(s)\phi(s)\|_{L_1} \Delta_{u\_ref} < \rho_r \qquad (52)$$

which implies that $||\omega_{ref\,\tau}||_{L\infty} < \rho_r$, thus contradicting (48). This finding proves the bound in (39).

Using (50), it follows the definition of the reference control in (34) that

$$
\begin{aligned}
&\left\| u_{a(c)\_ref_\tau} \right\|_{L_\infty} \\
&\leq \| C(s) \|_{L_1} \left(\| \phi(s) \|_{L_1} \left(L_{\rho r} \rho_r + B_L \right) + \left\| k_g \omega_d \right\|_{L_\infty} \right) \\
&= \rho_{ur}
\end{aligned}
\tag{53}
$$

and the proof is complete.

Considering that the reference system is assumed that the system's uncertainties are precisely known, so it is mainly used for analysis.

We define

$$
\rho = \rho_r + \bar{\gamma}_1
\tag{54}
$$

and let γ_1 be given by

$$
\gamma_1 = \frac{\| (1 - C(s)) H_0(s) \|_{L_1} \| \Delta u \|_{L_\infty}}{1 - \| G(s) \|_{L_1} L_{\rho r}} + \sigma
$$
$$
+ \frac{\| C(s) \|_{L_1} \gamma_0 + \| H_0(s) \|_{L_1} \Delta_{u\_ref}}{1 - \| G(s) \|_{L_1} L_{\rho r}}
\tag{55}
$$

where σ and γ_0 are arbitrary small positive constants such that $\gamma_1 \leq \bar{\gamma}_1$. Moreover, let

$$
\rho_{ur} \triangleq \rho_{ur} + \gamma_2
\tag{56}
$$

where ρ_{ur} is defined in (53) and γ_2 is defined as

$$
\gamma_2 = \| C(s)\phi(s) \|_{L_1} L_{\rho r} \gamma_1 + \| C(s)\phi(s)(sI - A_m) \|_{L_1} \gamma_0
$$
$$
+ \| C(s) \|_{L_1} \| \Delta u \|_{L_\infty}
\tag{57}
$$

The system dynamics in (22) and the state predictor in (24) lead to the following prediction error dynamics:

$$
\dot{\tilde{\omega}}(t) = A_m \tilde{\omega}(t) + B_m \Delta u(t) + \tilde{\eta}(t)
\tag{58}
$$

where $\Delta u(t) = u_{a(c)}(t) - u_a(t)$, $\tilde{\eta}(t) = \hat{\eta}(t) - \eta(t)$ and $\eta(t) = f(t, \omega(t))$.

Lemma 3: Given the system in (22) and the L_1 adaptive controller defined via (24-29), if $||\omega_\tau||_{L\infty} \leq \rho$ and $||u_{a(c)\tau}||_{L\infty} \leq \rho_u$, then, the prediction error $\tilde{\omega}(t)$ is uniformly bounded as (59), as shown at the bottom of this page.

Proof: Consider the following Lyapunov function candidate:

$$
V(t) = \frac{1}{2\Gamma} \tilde{\omega}^T(t) P \tilde{\omega}(t)
\tag{60}
$$

Since $\tilde{\omega}(0) = 0$, we have $V(0) = 0$. Taking the derivative of (60), we obtain the following:

$$
\begin{aligned}
\dot{V}(t) &= \frac{1}{2\Gamma} \left(\dot{\tilde{\omega}}^T(t) P \tilde{\omega}(t) + \tilde{\omega}^T(t) P \dot{\tilde{\omega}}(t) \right) \\
&= \frac{1}{2\Gamma} \left(\begin{array}{c} (A_m \tilde{\omega}(t) + B_m \Delta u(t) + \tilde{\eta}(t))^T P \tilde{\omega}(t) \\ + \tilde{\omega}^T(t) P (A_m \tilde{\omega}(t) + B_m \Delta u(t) + \tilde{\eta}(t)) \end{array} \right) \\
&= -\frac{1}{2\Gamma} \tilde{\omega}^T(t) Q \tilde{\omega}(t) + \frac{1}{\Gamma} \tilde{\omega}^T(t) P \left(\hat{\eta}(t) - \eta(t) \right) \\
&\quad + \frac{1}{\Gamma} \tilde{\omega}^T(t) P B_m \Delta u(t)
\end{aligned}
\tag{61}
$$

Substituting the adaptation law in (25) for $\hat{\eta}(t)$, we obtain the following:

$$
\begin{aligned}
&\dot{V}(t) \\
&= -\frac{1}{2\Gamma} \tilde{\omega}^T(t) Q \tilde{\omega}(t) + \frac{1}{\Gamma} \tilde{\omega}^T(t) P B_m \Delta u(t) \\
&\quad + \frac{1}{\Gamma} \tilde{\omega}^T(t) P \left(-\Gamma \tilde{\omega}(t) + \Gamma \kappa \hat{\Delta} u(t) - \eta(t) \right) \\
&= -\frac{1}{2\Gamma} \tilde{\omega}^T(t) Q \tilde{\omega}(t) - \tilde{\omega}^T(t) P \tilde{\omega}(t) - \frac{1}{\Gamma} \tilde{\omega}^T(t) P \eta(t) \\
&\quad + \frac{1}{\Gamma} \tilde{\omega}^T(t) P B_m \left(u_{a(c)}(t) + u_m(t) - u_{max} sat \left(\frac{u_c(t)}{u_{max}} \right) \right) \\
&\quad + \frac{1}{\Gamma} \tilde{\omega}^T(t) P \Gamma \kappa \hat{\Delta} u(t)
\end{aligned}
\tag{62}
$$

Defining $\| \eta_\tau \|_{L\infty} \leq L_\rho \rho + B_L = \bar{\eta}$, then

$$
\begin{aligned}
\dot{V}(t) &\leq -\tilde{\omega}^T(t) P \tilde{\omega}(t) \\
&\quad + \frac{1}{\Gamma} \| \tilde{\omega} \| \| P \|_2 \left(\| B_m \|_2 \left(u_{max} + \rho_u + \| u_m \|_{L_\infty} \right) \right. \\
&\quad \left. + \Gamma \kappa \left\| \hat{\Delta} u \right\|_{L_\infty} + \bar{\eta} \right)
\end{aligned}
\tag{63}
$$

Thus, for $t \in [0, \tau]$

$$
\begin{aligned}
&\| \tilde{\omega}(t) \| \\
&> \frac{\| P \|_2 (\| B_m \|_2 (u_{max} + \rho_u + \| u_m \|_{L_\infty}) + \Gamma \kappa \| \hat{\Delta} u \|_{L_\infty} + \bar{\eta})}{\Gamma \lambda_{min}(P)} \\
&\Rightarrow \dot{V}(t) < 0
\end{aligned}
\tag{64}
$$

If at any time $t_1 \in [0, \tau]$ (65), as shown at the bottom of the next page. Then,

$$
\begin{aligned}
&\frac{1}{2\Gamma} \lambda_{max}(P) \\
&\left(\frac{\| P \|_2 (\| B_m \|_2 (u_{max} + \rho_u + \| u_m \|_{L_\infty}) + \Gamma \kappa \| \hat{\Delta} u \|_{L_\infty} + \bar{\eta})}{\Gamma \lambda_{min}(P)} \right)^2 \\
&< V(t_1) = \frac{1}{2\Gamma} \tilde{\omega}(t_1)^T P \tilde{\omega}(t_1) \leq \frac{1}{2\Gamma} \lambda_{max}(P) \| \tilde{\omega}(t_1) \|^2
\end{aligned}
\tag{66}
$$

$$
\| \tilde{\omega}_\tau \|_{L\infty} \leq \sqrt{\frac{\lambda_{max}(P)}{\lambda_{min}^3(P)}} \left(\frac{\| P \|_2 \left(\| B_m \|_2 \left(u_{max} + \rho_u + \| u_m \|_{L_\infty} \right) + \Gamma \kappa \left\| \hat{\Delta} u \right\|_{L_\infty} + \bar{\eta} \right)}{\Gamma} \right)
\tag{59}
$$

which results in $\|\tilde{\omega}(t)\|$

$\|\tilde{\omega}(t)\|$

$$> \frac{\|P\|_2 \left(\|B_m\|_2 \left(u_{max} + \rho_u + \|u_m\|_{L_\infty} \right) + \Gamma\kappa \left\| \hat{\Delta}u \right\|_{L_\infty} + \bar{\eta} \right)}{\Gamma\lambda_{min}(P)}$$

because $\dot{V}(t_1) < 0$.

Then it follows that

$$V(t) \leq \frac{1}{2\Gamma}\lambda_{max}(P)$$

$$\left(\frac{\|P\|_2 \left(\|B_m\|_2 \left(u_{max} + \rho_u + \|u_m\|_{L_\infty} \right) + \Gamma\kappa \left\| \hat{\Delta}u \right\|_{L_\infty} + \bar{\eta} \right)}{\Gamma\lambda_{min}(P)} \right)^2$$

$$\forall t \in [0, \tau] \quad (67)$$

Since $\frac{1}{2\Gamma}\lambda_{min}(P)\|\tilde{\omega}(t)\|^2 \leq V(t)$, it follows that (68), as shown at the bottom of the this page. and the proof is complete.

Using the lemmas developed before, we can conclude that the state of the plant and the state of the reference system are bounded as follows.

Theorem 1: Consider the closed-loop reference system in (33-35) and the closed-loop system consisting of the system in (22) and the L_1 adaptive controller in (24-29) subject to the L_1-norm condition (37). If the adaptive gain is chosen to verify the design constraints

$$\Gamma \geq \sqrt{\frac{\lambda_{max}(P)}{\lambda_{min}^3(P)}}$$

$$\times \left(\frac{\|P\|_2 \left(\|B_m\|_2 (u_{max} + \rho_u + \|u_m\|_{L_\infty}) + \Gamma\kappa\|\hat{\Delta}u\|_{L_\infty} + \bar{\eta} \right)}{\gamma_0} \right)$$

$$(69)$$

then we have

$$\|\tilde{\omega}\|_{L_\infty} \leq \gamma_0 \quad (70)$$

$$\|\omega_{ref} - \omega\|_{L_\infty} \leq \gamma_1 \quad (71)$$

$$\|u_{a(c)\_ref} - u_{a(c)}\|_{L_\infty} \leq \gamma_2 \quad (72)$$

Proof: The proof is done by contradiction. Assume that the bounds (71) and (72) do not hold. Then, since $\|\omega_{ref}(0) - \omega(0)\|_\infty = 0 < \gamma_1$; $u_{a(c)\_ref}(0) - u_{a(c)}(0) = 0$; and

$\omega(t)$, $\omega_{ref}(t)$, $u_{a(c)}(t)$, and $u_{a(c)\_ref}(t)$ are continuous, $\tau > 0$ exists such that

$$\|\omega_{ref}(t) - \omega(t)\|_\infty < \gamma_1, \quad \|u_{a(c)\_ref}(t) - u_{a(c)}(t)\|_\infty$$
$$< \gamma_2 \forall t \in [0, \tau)$$

and

$$\|\omega_{ref}(\tau) - \omega(\tau)\|_\infty = \gamma_1,$$

or

$$\|u_{a(c)\_ref}(\tau) - u_{a(c)}(\tau)\|_\infty = \gamma_2$$

which implies that at least one of the following equalities holds:

$$\|(\omega_{ref} - \omega)_\tau\|_{L_\infty} = \gamma_1, \quad \|(u_{a(c)\_ref} - u_{a(c)})_\tau\|_{L_\infty} = \gamma_2 \quad (73)$$

Taking into consideration the definitions of ρ and ρ_u in (54) and (56), it follows from Lemma 2 and the equalities in (69) that

$$\|\omega_\tau\|_{L_\infty} \leq \rho, \quad \|u_{a(c)\tau}\|_{L_\infty} \leq \rho_u \quad (74)$$

These bounds imply that the assumption of Lemma 3 holds. Then, selecting the adaptation gain Γ according to the design constraint in (73), it follows that

$$\|\tilde{\omega}\|_{L_\infty} \leq \gamma_0 \quad (75)$$

The response of the closed-loop system in the frequency domain consequently takes the following form:

$$\omega(s) = G(s)\eta(s) - C(s)H(s)\phi(s)\tilde{\eta}(s)$$
$$+ C(s)H(s)k_g\omega_d(s) - H_0(s)\Delta u(s) \quad (76)$$

This expression together with the response of the closed-loop reference system in (33) yields

$$\omega_{ref}(s) - \omega(s) = G(s)\left(\eta_{ref}(s) - \eta(s)\right) + C(s)\tilde{\omega}(s)$$
$$+ H_0(s)\Delta u(s)(1 - C(s)) - H_0(s)\Delta u_{ref}(s)$$
$$(77)$$

We have (78)–(80), as shown at the bottom of the next page, which contradicts the first equality in (73).

To show that the second equality in (73) also cannot hold, we notice from (28) and (34) that one can derive the following:

$$u_{a(c)\_ref}(s) - u_{a(c)}(s)$$
$$= -C(s)\left(\phi(s)\eta_{ref}(s) - \phi(s)\eta(s) - \phi(s)\tilde{\eta}(s)\right) \quad (81)$$

$$V(t_1) > \frac{1}{2\Gamma}\lambda_{max}(P) \left(\frac{\|P\|_2 \left(\|B_m\|_2 \left(u_{max} + \rho_u + \|u_m\|_{L_\infty} \right) + \Gamma\kappa\|\hat{\Delta}u\|_{L_\infty} + \bar{\eta} \right)}{\Gamma\lambda_{min}(P)} \right)^2 \quad (65)$$

$$\|\tilde{\omega}_\tau\|_{L_\infty} \leq \sqrt{\frac{\lambda_{max}(P)}{\lambda_{min}^3(P)}} \left(\frac{\|P\|_2 \left(\|B_m\|_2 \left(u_{max} + \rho_u + \|u_m\|_{L_\infty} \right) + \Gamma\kappa \left\| \hat{\Delta}u \right\|_{L_\infty} + \bar{\eta} \right)}{\Gamma} \right) \quad (68)$$

TABLE 3. Areas of different portions.

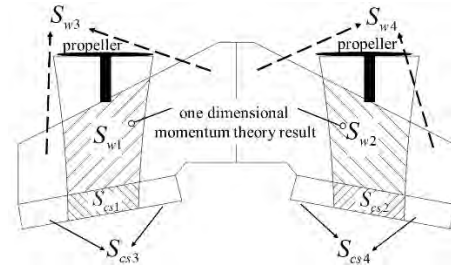| Parameter	Description	Value
$S_{w1}(S_{w2})$	Area within slipstream (wing)	0.0247 m^2
$S_{w3}(S_{w4})$	Area out of slipstream (wing)	0.05595 m^2
$S_{cs1}(S_{cs2})$	Area within slipstream (control surface)	0.0058 m^2
$S_{cs3}(S_{cs4})$	Area out of slipstream (control surface)	0.0198 m^2

$$u_{a(c)\_ref}(s) - u_{a(c)}(s)$$
$$= -C(s)\phi(s)\left(\eta_{ref}(s) - \eta(s)\right)$$
$$+ C(s)\phi(s)(sI - A_m)\,\tilde{\omega}(s) - C(s)\Delta u(s) \quad (82)$$

$$\left\|\left(u_{a(c)\_ref} - u_{a(c)}\right)_\tau\right\|_{L_\infty}$$
$$\leq \|C(s)\phi(s)\|_{L_1} L_{\rho_r} \left\|(\omega_{ref} - \omega)_\tau\right\|_{L_\infty}$$
$$+ \|C(s)\phi(s)(sI - A_m)\|_{L_1} \gamma_0 + \|C(s)\|_{L_1} \|\Delta u\|_{L_\infty} \quad (83)$$

$$\left\|\left(u_{a(c)\_ref} - u_{a(c)}\right)_\tau\right\|_{L_\infty}$$
$$\leq \|C(s)\phi(s)\|_{L_1} L_{\rho_r}(\gamma_1 - \sigma) + \|C(s)\phi(s)(sI - A_m)\|_{L_1} \gamma_0$$
$$+ \|C(s)\|_{L_1} \|\Delta u\|_{L_\infty} < \gamma_2 \quad (84)$$

which contradicts the second equality in (73). These findings prove the bounds in (71-72) and the proof is complete.

V. SIMULATIONS

In this section, digital simulations of attitude tracking of the dual-rotor tail sitter are presented to demonstrate the effectiveness of the proposed method in this study. The simulation environments are introduced first, and the results are given later.

A. SIMULATION ENVIRONMENTS

During the hover stage, the aerodynamic forces and moments are produced mainly within the slipstreams of the propellers; therefore, one-dimensional momentum theory is used to analyze the effects of the control surfaces. As shown in Figure 3, the wings and control surfaces can be mainly divided into two areas, which are the areas within the slipstream and areas outside the slipstream. The areas of different portions are listed in Table 3.

The propeller induced velocity V_{slip} near control surfaces during hover stage can be calculated as 14m/s by using

FIGURE 3. Propeller slipstream partition.

momentum theory [12]. Then, the maximal pitch and yaw control moments generated by the control surfaces can be calculated as

$$\left|u_{max(pitch)}\right|$$
$$= \frac{1}{2}\rho V_{slip}^2 (S_{w1} + S_{w2} + S_{cs1} + S_{cs2}) c \left|C_{m\delta_e}\right| \delta_{e(max)} \frac{\pi}{180}$$
$$= 0.5 \times 1.225 \times 14^2 \times 0.061 \times 0.253 \times 0.2857 \times 20/57.3$$
$$= 0.1848 N \cdot m$$

$$\left|u_{max(yaw)}\right|$$
$$= \frac{1}{2}\rho V_{slip}^2 (S_{w1} + S_{w2} + S_{cs1} + S_{cs2}) b \left|C_{n\delta_e}\right| \delta_{e(max)} \frac{\pi}{180}$$
$$= 0.5 \times 1.225 \times 14^2 \times 0.061 \times 0.8774 \times 0.1562 \times 20/57.3$$
$$= 0.35 N \cdot m$$

Note that C_{m0} in Table 2 is -0.036, which means an initial nose-down pitching moment of approximately -0.0667 N·m when the angle of attack is near 0°. The maximal thrust the two motors can offer is 1.25 kg while the weight of the UAV is 0.81 kg, which means approximately 50% thrust margins during hover. Therefore, thrust saturation, which means roll control saturation, is not considered here. In this study, we mainly investigate the performance of a closed-loop system in pitch and yaw angle tracking when input constraints of control surfaces exist. The initial values of the vehicle and predictors of the L_1 adaptive controllers are listed in Table 4.

The dynamics of the actuators in Figure 2 are considered as first-order systems with certain time delays. According to

$$\left\|(\omega_{ref} - \omega)_\tau\right\|_{L_\infty} \leq \|G(s)\|_{L_1} L_{\rho_r} \left\|(\omega_{ref} - \omega)_\tau\right\|_{L_\infty} + \|C(s)\|_{L_1} \|\tilde{\omega}_\tau\|_{L_\infty}$$
$$+ \|(1 - C(s)) H_0(s)\|_{L_1} \|\Delta u\|_{L_\infty} + \|H_0(s)\|_{L_1} \left\|\Delta u_{ref}\right\|_{L_\infty} \quad (78)$$

$$\left\|(\omega_{ref} - \omega)_\tau\right\|_{L_\infty} \leq \frac{\|(1 - C(s)) H_0(s)\|_{L_1} \|\Delta u\|_{L_\infty}}{1 - \|G(s)\|_{L_1} L_{\rho_r}}$$
$$+ \frac{\|H_0(s)\|_{L_1} \left\|\Delta u_{ref}\right\|_{L_\infty} + \|C(s)\|_{L_1} \|\tilde{\omega}_\tau\|_{L_\infty}}{1 - \|G(s)\|_{L_1} L_{\rho_r}} \quad (79)$$

$$\left\|(\omega_{ref} - \omega)_\tau\right\|_{L_\infty} \leq \frac{\|C(s)\|_{L_1} \gamma_0 + \|(1 - C(s)) H_0(s)\|_{L_1} \|\Delta u\|_{L_\infty} + \|H_0(s)\|_{L_1} \Delta_{u\_ref}}{1 - \|G(s)\|_{L_1} L_{\rho_r}}$$
$$= \gamma_1 - \sigma < \gamma_1 \quad (80)$$

Parameter	Description	Value
ω_0	angular rates	$[0,0,0]$ °/s
$\hat{\omega}_0$	angular rates of state predictor in L_1 adaptive controller	$[0,0,0]$ °/s
Ω_0	Euler angle	$[0,0,0]$ °
δ_e	control surface deflection	$[-6, -6]$ °

previous studies [34], the dynamics of control surfaces and motors can be modeled as $1/(0.03s + 1)$ and $1/(0.02s + 1)$, respectively. The time delays of the system mainly come from the following sources: control loop frequency and discrete sampling, dynamics of data fusion and time delays from the actuators. According to previous experiences with flight tests, at least 20 ms input time delay margins are needed for the controller. Therefore, time delays of 25 ms in the control input are used in the following simulations.

B. CONTROLLER PARAMETER SELECTION
For the feedforward compensator mentioned in (10), the choices of α_1, α_2, and α_3 should not be too ambitious to avoid overcompensation. The inertial coupling terms $\omega \times J\omega$ are deduced from Newton-Euler equations and are used widely in aircraft modeling, so they can be treated as high-confidence terms; thus, α_1 is chosen to be 0.6. Considering the finite model precision, the aerodynamic-related parameters α_2 and α_3 are chosen to be 0.3 and 0.4, respectively.

For the baseline LQR controller mentioned in equation (17), the matrices Q and R are chosen as follows to offer good performance for a nominal system in equation (13).

$$Q = \begin{bmatrix} 0.15 & 0 & 0 & 0 & 0 & 0 \\ 0 & 0.02 & 0 & 0 & 0 & 0 \\ 0 & 0 & 0.15 & 0 & 0 & 0 \\ 0 & 0 & 0 & 0.005 & 0 & 0 \\ 0 & 0 & 0 & 0 & 0.001 & 0 \\ 0 & 0 & 0 & 0 & 0 & 0.005 \end{bmatrix}$$

$$R = \begin{bmatrix} 0.8 & 0 & 0 \\ 0 & 0.8 & 0 \\ 0 & 0 & 0.8 \end{bmatrix}$$

From equation $A_m = -B_m K_2$ and using the results from the ARE in (18), we obtain the following:

$$A_m = \begin{bmatrix} -6.6814 & 0 & 0 \\ 0 & -8.4075 & 0 \\ 0 & 0 & -7.2304 \end{bmatrix}$$

which defines the desired dynamics of the angular rates for the inner L_1 adaptive controller.

For the L_1 adaptive controller, the adaptive gain Γ is chosen to be 300, because in the simulation, we don't need to particularly consider the performance of the autopilot hardware and higher adaptive gain would be beneficial to the system performance. $D(s)$ is chosen to be $1/s$, $K_f = 10 \cdot I_{3\times3}$ and $\kappa = 10$. The parameter K_f reflects the bandwidth of

low-pass filter and it decides the tradeoff between robustness and performance of L_1 adaptive control architecture. To guarantee enough time-delay margin of the closed-loop system, the bandwidth is defined as 10rad/s. The parameter κ defines how fast that we want the system out of saturation and overlarge value may hurt adaptation.

C. ATTITUDE TRACKING SIMULATION
Simulation comparisons are made between the L_1 adaptive control architecture proposed by Vanness *et al.* [30] and the method we propose in this study. We define these two architectures as follows.

M1: L_1 adaptive control architectures proposed by Vanness *et al.* [30] that does not consider the input constraints during the controller design process.

M2: The method we propose in this study with consideration of the input constraints during the controller design process.

1) ATTITUDE TRACKING PERFORMANCE WITHOUT MAXIMAL DEFLECTION OF CONTROL SURFACES
To illustrate the basic performance of the closed-loop system, the following simulations are first performed when there are no maximal deflections of control surfaces, leading to the same performance of M1 and M2 because the input saturation protective mechanisms are not triggered in M2. The roll, pitch and yaw command signals are defined as square waves with the amplitude of 0.3 rad, 0.45 rad and 0.27 rad respectively. The periods of roll, pitch and yaw command signals are 15 s, 20 s and 15 s respectively.

The simulation results are shown in Figure 4 where RES and CMD denotes the response of system and the command signals respectively. The deflection of control surface 1 and control surface 2 are defined as cs1 and cs2 respectively. Without special statement, the definitions of symbols in figures are all the same within this manuscript.

All actuators are within the normal operating conditions, and no maximal deflection of control surfaces occur. The deflections of the control surface and thrust variations are relatively gentle, and no chattering exists. As mentioned in Section IV.A, there is approximately -0.0667N · m aerodynamic pitch moment generated by the wing when the angle of attack is near $0°$, so the control surfaces always need to deflect approximately $-6°$ to generate the corresponding control moment for compensation. The coupling effects among roll, pitch and yaw can be observed, and there are mainly two factors causing these effects. The first factor is the inertial coupling terms $\omega \times J\omega$ in (2) and the second factor is the coupling operation of the control surfaces between pitch and yaw. When the control surfaces are executing symmetry deflections in response to pitch command, extra yaw command would need control surfaces to deflect asymmetry, which will inevitably affect the pitch response and vice versa. In general, it can be seen from the simulation results that static tracking errors near $0°$ and the Euler angle can rapidly
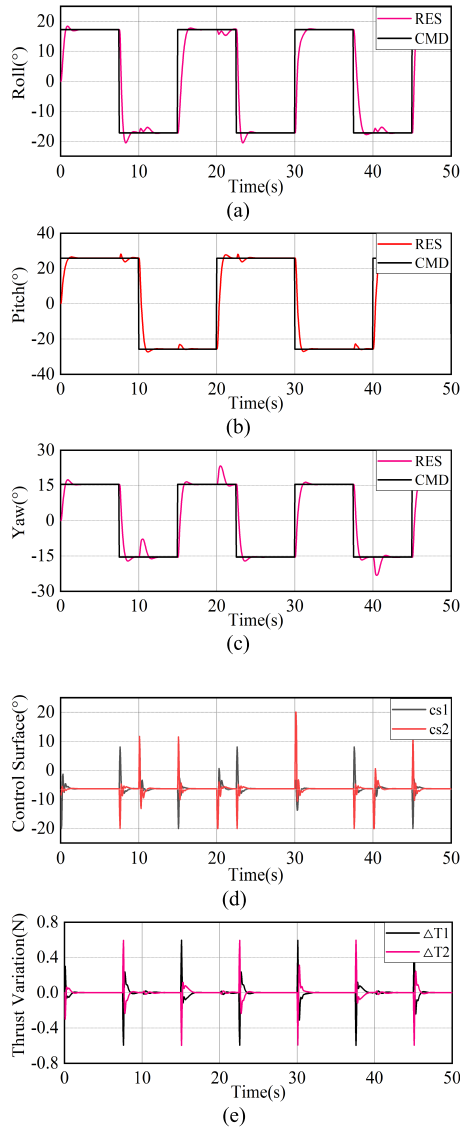
FIGURE 4. Attitude tracking without maximal deflection of control surfaces. (a) Roll angle tracking. (b) Pitch angle tracking. (c) Yaw angle tracking. (d) Control surface deflections. (e) Thrust variations.

track the command signal which means good performance of a closed-loop system.

2) PITCH ATTITUDE TRACKING PERFORMANCE WITH MAXIMAL DEFLECTION OF CONTROL SURFACES

In this section, the attitude tracking performance of M1 and M2 is compared when maximal deflection of control surfaces exists. Considering that pitch and yaw control are coupled, only pitch angle tracking is tested here to better illustrate the performance of these two methods. The pitch command signals are defined as square waves with the amplitude of 0.9 rad and the periods is 20 s. Constant disturbance moments are used to test the system's ability to compensate for uncertainties, and pitch disturbance moments of -0.08 N $\cdot$ m are added to the system at simulation time $t = 4$ s. Considering that the deflections of the control surfaces may not
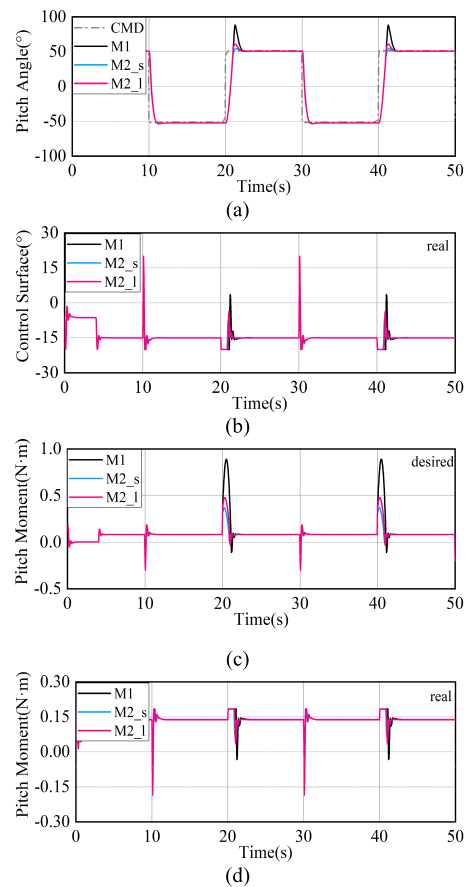
FIGURE 5. Pitch attitude tracking with maximal deflection of control surfaces. (a) Pitch angle tracking. (b) Control surface deflections. (c) Desired pitch control moments calculated by the controller. (d) Actual generated pitch control moments.

be measured, the estimated maximal control moments are used instead in M2. Furthermore, the real control moments that the control surface can generate may also not be known accurately; the chosen maximal control moments may be larger or smaller than the real maximal control moments, so both cases are tested in the following simulations. From Section IV.A, we know the maximal pitch control moment is $u_{max(pitch)} = 0.1848$ N $\cdot$ m; thus, in simulation M2_s, we define $u_{max(pitch)}^{est} = 0.15$ N $\cdot$ m and in simulation M2_l, we define $u_{max(pitch)}^{est} = 0.3$ N $\cdot$ m.

From the simulation results, we can see that regardless of whether $u_{max(pitch)}^{est}$ is chosen to be larger or smaller than its true value in a certain range, the attitude tracking of M2_s and M2_l always shows better performance than that of M1. When control surface saturation occurs at time $t = 20$ s, the overshoot of M1 is 36° while the overshoots of M2_s and M2_l are both less than 10°, which is substantial improvement. In addition, from the pitch angle tracking results, we can also see that M2_s shows better performance than M2_l and the reason is that when saturations occur, M2_s could make the system move out of saturation more quickly, while M2_l seems to feel this saturation lag behind because

a larger estimated value would make the anti-windup mechanism trigger only after saturation has already occurred. However, the value of $u_{max(pitch)}^{est}$ should not be chosen to be too small; otherwise, premature compensation will restrain the control output and degrade the performance of the closed-loop system.

3) PITCH AND YAW ATTITUDE TRACKING PERFORMANCE WITH MAXIMAL DEFLECTION OF CONTROL SURFACES

In this section, both pitch and yaw angle tracking are tested simultaneously to verify the performance of the proposed method. The pitch and yaw command signals are defined as square waves with the amplitude of 0.6 rad and 0.54 rad respectively and the periods of pitch and yaw command signals are 20 s and 15 s respectively. Considering that pitch control and yaw control are coupled, the estimated maximal pitch and yaw control moments are chosen as $u_{max(pitch)}^{est} = 0.15N \cdot m$ and $u_{max(yaw)}^{est} = 0.3N \cdot m$ respectively, which are both smaller than their true values. Extra pitch disturbance moments of -0.08 N $\cdot$ m and yaw disturbance moments of -0.04 N $\cdot$ m are also added to the system at simulation time $t = 4$ s and $t = 13$ s respectively.

From the simulation results, we can see that M2 still has the ability to reduce the overshoot of the system's response even if the pitch and yaw angle are tracked simultaneously. At time t_0, it can be intuitively explained why M2 shows better performance. We can see from the control surface deflection after time t_0, that the control surface 1 of M2 starts to deflect in reverse, while the deflection of M1 still holds at approximately 20°. This effect can be seen more clearly from the time history of the actual generated control moments; just after time t_0, the pitch moment that M1 generates is still 0.16 N $\cdot$ m, while the pitch moment of M2 is beginning to decrease, therefore causing less overshoots. A similar phenomenon could also be observed at simulation time t_1. Besides, from the control deficiency, which is defined in equation (27), in pitch and yaw, we can find that with the anti-windup protection mechanism in M2, the differences between desired control moments and real control moments are smaller and disappear faster which could help control surface out of saturation quickly.

Furthermore, we also test the performances when the estimated control moments are chosen to be smaller, so $u_{max(pitch)}^{est}$ and $u_{max(yaw)}^{est}$ are set as 0.15 N $\cdot$ m and 0.1 N $\cdot$ m, respectively. In this simulation, the pitch and yaw command signals are defined as square waves with the amplitude of 0.6 rad and 0.45 rad respectively and the periods of pitch and yaw command signals are 20 s and 15 s respectively. The simulation results are shown in Figure 7. M2_nm and M2_rd denote the results for $u_{max(yaw)}^{est}$ values of 0.3 N $\cdot$ m and 0.1 N $\cdot$ m respectively. It is interesting to note from Figure 7(b) that although the performance of closed-loop system improves, the response of M2_rd seems to lag behind the response of M2_nm which is an adverse effect when $u_{max(yaw)}^{est}$ is chosen to be smaller. Furthermore, if u_{max}^{est} is chosen to be too small,
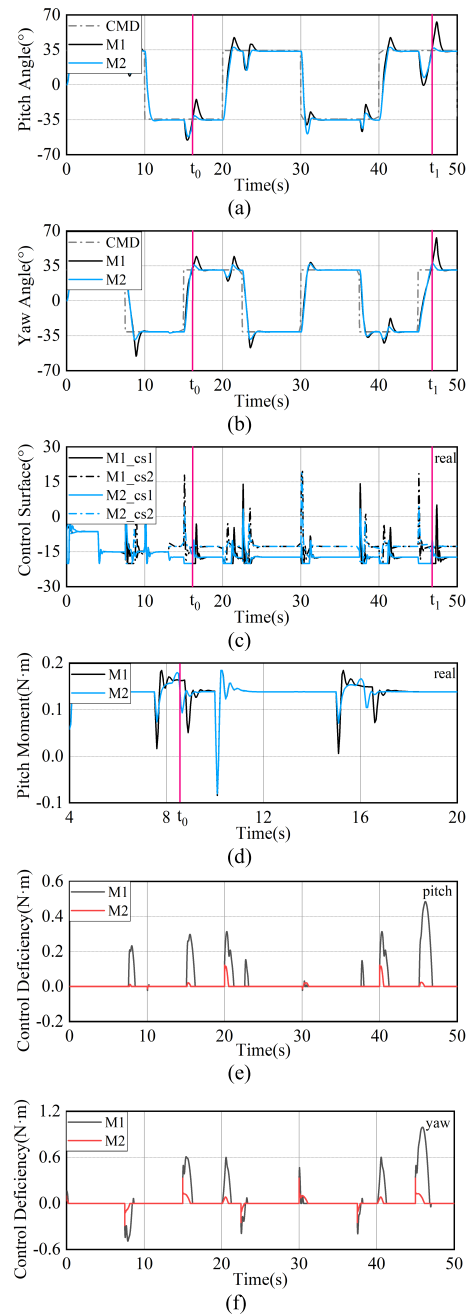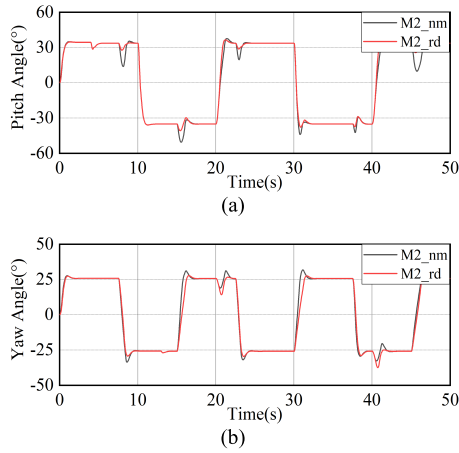

FIGURE 6. Pitch and yaw attitude tracking with maximal deflection of control surfaces. (a) Pitch angle tracking. (b) Yaw angle tracking. (c) Actual control surface deflections. (d) Actual generated control moments. (e) Control deficiency in pitch. (f) Control deficiency in yaw.

static error could occur in the attitude tracking response and this should definitely be avoided in a real flight test.

4) ATTITUDE TRACKING PERFORMANCE WITH CONTROL SURFACE FAILURE

In this section, the attitude tracking performance is tested when control surface failure occurs. The pitch and yaw command signals are defined as square waves with the amplitude of 0.6 rad and 0.45 rad respectively and the periods of pitch

FIGURE 7. Comparison of attitude tracking. (a) Pitch angle Tracking. (b) Yaw angle tracking.
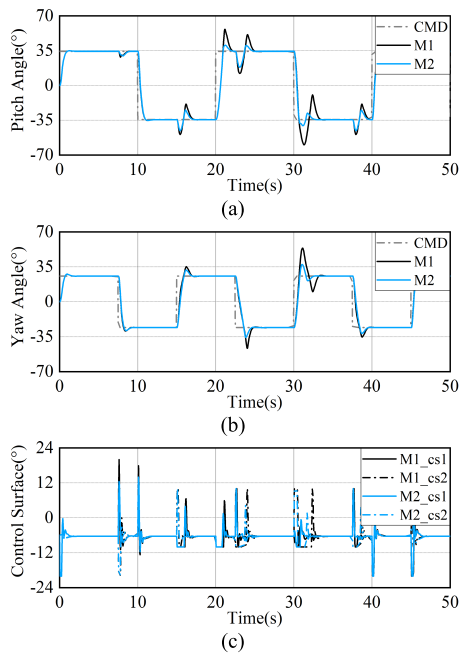

FIGURE 8. Attitude tracking with control surface failure. (a) Pitch angle tracking. (b) Yaw angle tracking. (c) Actual control surface deflections.

and yaw command signals are 20 s and 15 s respectively It is assumed that the maximal deflections of both control surfaces are restrained to $\pm 10°$ from simulation time $t = 12 - 40$ s and no extra disturbance moments were added.

It can be seen that during time interval $t = 12 - 40$ s, both performances degrade because of control surface failure. However, the proposed method in this study still shows better performance than that of M1. In other words, the method proposed in this study could improve the system performance effectively when there exits control surface failure, which could better guarantee the flight safety of UAV.

FIGURE 9. Flight tests.

VI. FLIGHT TEST RESULTS

Flight tests were conducted continuously in an open space, as shown in Figure 9. Pixhawk [36] was used as the autopilot of the tail-sitter in this study. The autopilot hardware is equipped with a sensor of 3-axis accelerometer/gyroscope MPU6000 to measure the original accelerated velocities and angular rates with sampling rates of approximately 1000Hz. Terrestrial magnetism is measured by an external magnetometer HMC5883 with sampling rates of nearly 150Hz. The extended Kalman filter (EKF) algorithm is used to estimate the attitude of the vehicle on on-line real-time process by taking advantage of these measurements from sensors. The algorithm takes 3-axis angular rate, 3-axis angular acceleration, 3-axis component of acceleration in the body frame and 3-axis component of magnetometer in the body frame as state variables. The measurements of accelerometer, gyroscope and magnetometer are defined as measurement matrix. One step prediction is calculated from the dynamic model and the predicted results are then modified by the measurement matrix to get smoothened and relatively accurate attitude estimates with little phase delay. The updating rate of EKF output was approximately 250Hz, which influenced the choice of adaptive gain Γ, and an overlarge adaptive gain would make the attitude shake by our flight test experiences.

The control parameters in real flight tests are specified as $\alpha_1 = 0.6$, $\alpha_2 = 0.2$, $\alpha_3 = 0.3$, $R = 0.8 \cdot I_{3\times3}$, $\Gamma = 160$, $D(s) = 1/s$, $K_f = 10 \cdot I_{3\times3}$, $\kappa = 5$.

$$Q = \begin{bmatrix} 0.3 & 0 & 0 & 0 & 0 & 0 \\ 0 & 0.1 & 0 & 0 & 0 & 0 \\ 0 & 0 & 0.3 & 0 & 0 & 0 \\ 0 & 0 & 0 & 0.01 & 0 & 0 \\ 0 & 0 & 0 & 0 & 0.003 & 0 \\ 0 & 0 & 0 & 0 & 0 & 0.01 \end{bmatrix}$$

For safety considerations, the estimated maximal control moments were chosen conservatively as $u^{est}_{max(pitch)} = 0.25$ N· m, and $u^{est}_{max(yaw)} = 0.3$ N · m in our flight test.

To test the performance when maximal defection of control surfaces exists, the following commands are given to the vehicle by the drone pilot. First, a pitch command is desired, and then a yaw command is added to the vehicle. After a few seconds, the vehicle is pulled back to its initial attitudes.
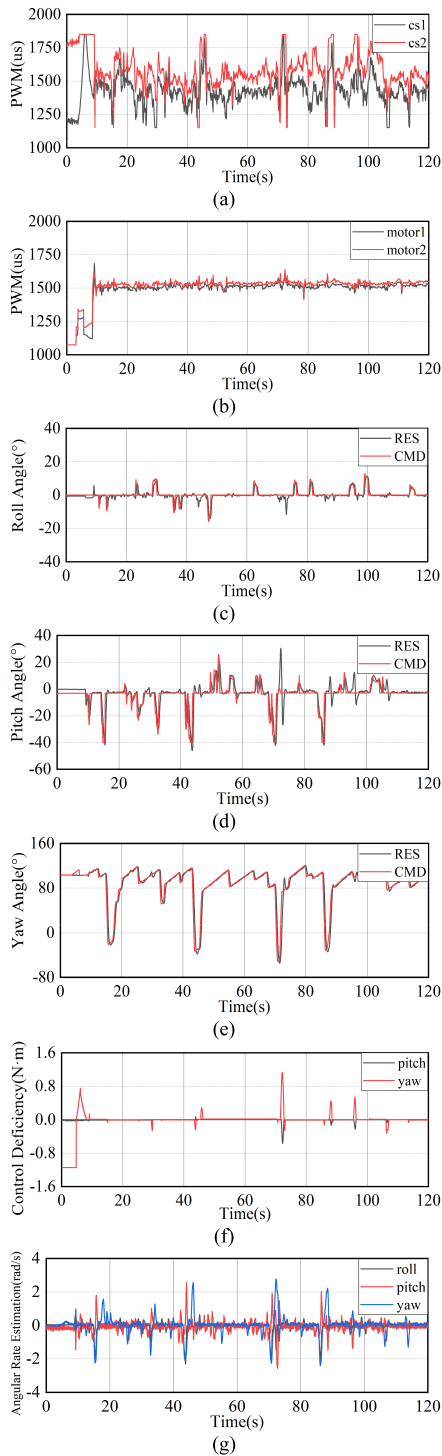
FIGURE 10. Attitude tracking performances with M1. (a) Control surfaces PWM. (b) Motors PWM. (c) Roll angle tracking. (d) Pitch angle Tracking. (e) Yaw angle tracking. (f) Control deficiency. (g) States of predictor.

A. FLIGHT TEST WITH METHOD M1

In this flight test, no input saturation protection mechanism was set with method M1. Figure 10 gives the time history of actuators' pulse width modulation (PWM) and the basic performance of attitude tracking.
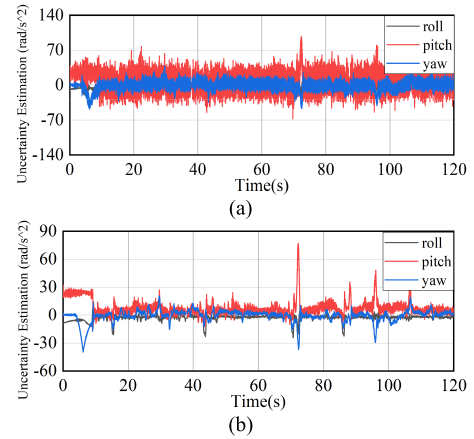

FIGURE 11. Uncertainties estimation. (a) Original data without smoothness. (b) Processed data after smoothness.
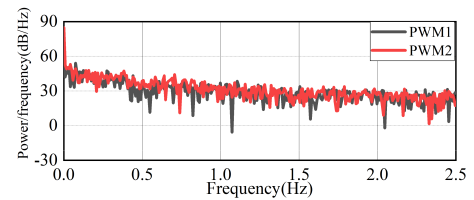

FIGURE 12. Power spectral density of control surfaces.

From the time history of motors' pulse width modulation (PWM) in Figure 10(b), we can see that roll attitude control can be realized by small differential thrust, so it is reasonable not to consider the roll control saturation as we mentioned before.

The closed-loop system shows good attitude tracking performance when no actuator saturations occur. However, from the time history of control surfaces' PWM, it is remarkable to see at time t = 73 s that maximal deflections occur and the performance degradation appears clearly in pitch angle tracking. An overshoot of 30° in pitch angle tracking can be seen at the beginning of time 73 s and this overshoot is inevitable because after control surfaces reached to its limit, no more control moments could be generated leading to the degradation of system performance. However, the continues time of the maximal deflections would make the control surfaces go into saturation. We can see that just after the 30° positive overshoot, a −27° negative overshoot showed up and these results are similar to the results in Figure 6. We can see that the reverse overshoots always exist after the control surface enters saturation and a similar phenomenon could also be observed at time t = 88 s, 96 s, and 106 s. Furthermore, the estimation of angular rates in Fig.10 (g) has the similar response with Euler angles and this indicates that the L_1 adaptive controller works well during the whole flight.

In this flight test with method M1, control deficiency $\hat{\Delta}u(t)$ is recorded but not used, and the consistent manifestation between the PWM of the control surfaces and $\hat{\Delta}u(t)$ means that the chosen values of $u_{max(pitch)}^{est}$ and $u_{max(yaw)}^{est}$ could
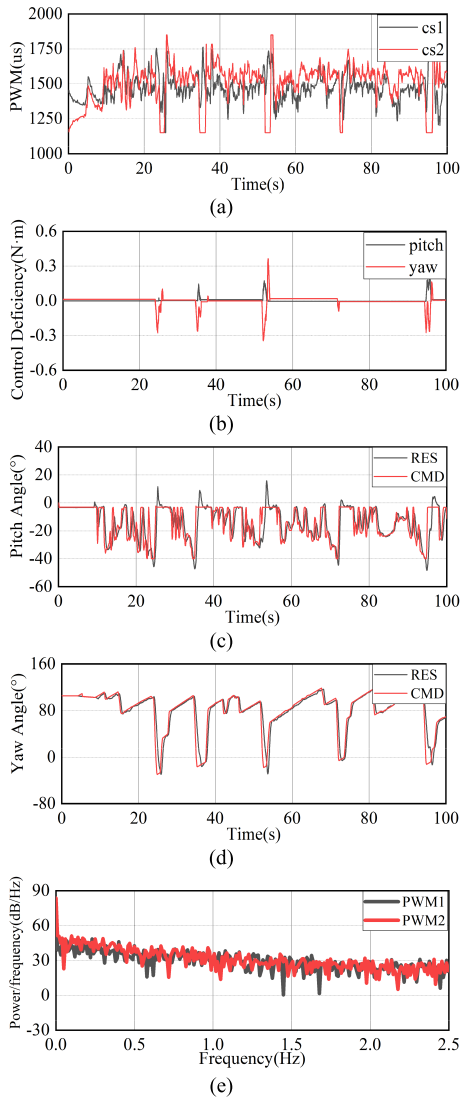
FIGURE 13. Flight test with M2. (a) Control surfaces PWM. (b) Control deficiency. (c) Pitch angle tracking. (d) Yaw angle tracking. (e) Power spectral density of control surfaces.

FIGURE 14. Repeatable experimental results with M1. (a) Pitch angle tracking in flight test 1. (b) Control deficiency in flight test 1. (c) Pitch angle tracking in flight test 2. (d) Control deficiency in flight test 2.

capture the situation if the control surfaces reach their limits effectively.

The uncertainty estimation and power spectral density of control surfaces are shown in Figure 11 and Figure 12 respectively.

From the results of uncertainty estimations $f(t, \omega(t))$ in Figure 11, we can see that at time t = 73 s, 88 s, 96 s, and 106 s, the controller could capture the uncertainties caused by control surfaces saturation. However, the tracking performance degradation can be seen obviously in Figure 10 because no input constraints is considered in the design process of method M1.

Furthermore, it is hard to say whether the deflections of control surfaces are gentle just from the time history of PWM in Figure 10 (a), so the power spectral density figure of PWM is drawn. Although the physical meaning may seem
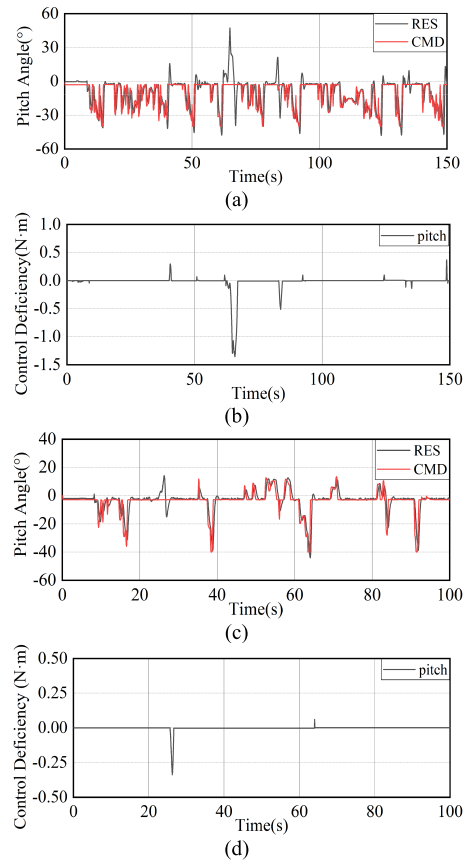
unclear, it could reflect the softness of the control surface outputs. Figure 12 shows that control signals concentrate in the low frequency region, and this concentration means that the deflections of the control surface are gentle and no chattering exists.

B. FLIGHT TEST WITH METHOD M2

The flight tests results with method M2 are shown in Figure 13. In this method, input saturation protection mechanism was designed to help to improve attitude tracking performance when there exists maximal deflection of control surfaces.

It can be seen the maximal deflection of control surfaces occurs at time $t = 24$ s, 35 s, 52 s, 73 s, and 95 s respectively from time history of PWM, which is also consistent with the results in control deficiency $\Delta\hat{u}(t)$. In this flight test, although we could see that the positive overshoots still occur when the control surfaces reach their limits, no negative overshoots exit with the help of the method proposed in this study. From the analysis of the power spectral density for PWM, we could see that the deflections of the control surface are gentle, which also indicates the good robustness of the closed-loop system.
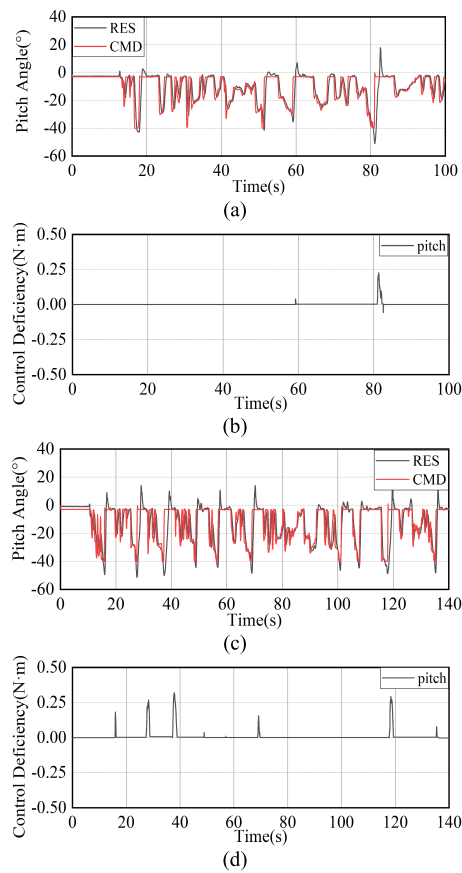
FIGURE 15. Repeatable experimental results with M2. (a) Pitch angle tracking in flight test 1. (b) Control deficiency in flight test 1. (c) Pitch angle tracking in flight test 2. (d) Control deficiency in flight test 2.

C. REPEATED FLIGHT TESTS

Finally, to illustrate that the experimental results are repeatable, several other flight tests were also conducted and some of them are shown below. Figure 14 and Figure 15 show two extra flight tests with method M1 and method M2 respectively. Control deficiencies are all recorded in these tests.

From the results of attitude tracking performance in Figure 14, similar phenomenon can be seen as it is in Figure 10. The controller with method M1 couldn't handle this situation well when there exists maximal deflection of control surfaces and the overshoots of pitch angle are relatively large.

From the flight results in Figure 15, the same conclusions could be made as before; that is the attitude tracking performance could always be improved by using the method we proposed in this study when the control surfaces enter saturation. Further, based on the whole flight tests, we can also find that the worst situation of control deficiency of M1 is near $1.5 N \cdot m$ while the control deficiency of M2 is always below $0.5 N \cdot m$, that is control deficiency of M1 is always larger than M2 under the similar manipulation from the drone pilot and this phenomenon is also consistent with the simulation results in Figure 6 (e) and this phenomenon

could explain why method M2 shows better performance than method M1 in an intuitive way.

VII. CONCLUSION

In this study, the problem of attitude tracking of the L_1 adaptive control architecture with input constraints is investigated. To address this problem, a novel L_1 adaptive control architecture is proposed in this article. The stability and performance bounds of the closed-loop system are analyzed to illustrate the impact of input constraints. From the simulation and flight test results, we can conclude that with the method proposed in this study, the overshoots could be eliminated as much as possible and this method improves the system performance considerably when maximal deflection of control surfaces exists. In addition, in a real-world experiment, we find that there exists a maximal value of adaptive gain that can be chosen according to the control loop running rate. An overlarge adaptive gain would make the vehicle shake while an overly small value could degrade the closed-loop performance.

In our current research, the estimated maximal control moments are chosen to be smaller than the maximal moments that can be generated when pitch or yaw control are considered separately. More in-depth studies on the control allocation of control surfaces may help to choose better estimated maximal control moments that could be benefit to system's performance. Furthermore, the studies on the influences of higher order filter to the system will also be explored in future studies.

REFERENCES

[1] R. Murphy and M. J. Shields, "Task force on the role of autonomy in the DoD systems," Defense Sci. Board, Washington, DC, USA, Tech. Rep. TR-10-01, Jul. 2012.

[2] S. Shkarayev, J.-M. Moschetta, and B. Bataille, "Aerodynamic design of micro air vehicles for vertical flight," *J. Aircr.*, vol. 45, no. 5, pp. 1715–1724, Sep./Oct. 2008.

[3] P. K. Lian and S. A. Wich, "Dawn of drone ecology: Low-cost autonomous aerial vehicles for conservation," *Tropical Conserv. Sci.*, vol. 5, no. 5, pp. 121–132, Jul. 2012.

[4] G. Notarstefano and J. Hauser, "Modeling and dynamic exploration of a tilt-rotor VTOL aircraft," *IFAC Proc. Volumes*, vol. 43, no. 14, pp. 119–124, Sep. 2010.

[5] G. D. Francesco and M. Mattei, "Modeling and incremental nonlinear dynamic inversion control of a novel unmanned tiltrotor," *J. Aircr.*, vol. 53, no. 1, pp. 73–86, Apr. 2015.

[6] H. Stone and K. C. Wong, "Preliminary design of a tandem-wing tail-sitter UAV using multi-disciplinary design optimization," in *Proc. AUVSI*, 1996, pp. 163–178.

[7] R. H. Stone, P. Anderson, C. Hutchison, A. Tsai, P. Gibbens, and K. C. Wong, "Flight testing of the t-wing tail-sitter unmanned air vehicle," *J. Aircr.*, vol. 45, no. 2, pp. 673–685, Mar/Apr. 2018.

[8] J. Forshaw and V. Lappas, "High-fidelity modeling and control of a twin helicopter rotor tailsitter," in *Proc. AIAA Guid., Navigat., Control Conf.*, Aug. 2011, pp. 1–15.

[9] J. L. Forshaw, V. J. Lappas, and P. Briggs, "Transitional control architecture and methodology for a twin rotor tailsitter," *J. Guid., Control, Dyn.*, vol. 37, no. 4, pp. 1289–1298, Sep. 2014.

[10] P.-R. Bilodeau and F. Wong, "Modeling and control of a hovering mini tail-sitter," *Int. J. Micro Air Veh.*, vol. 2, no. 4, pp. 211–220, Dec. 2010.

[11] S. Verling, B. Weibel, M. Boosfeld, K. Alexis, M. Burri, and R. Siegwart, "Full attitude control of a VTOL tailsitter UAV," in *Proc. IEEE Int. Conf. Robot. Autom. (ICRA)*, Stockholm, Sweden, May 2016, pp. 3006–3012.

[12] W. Khan and M. Nahon, "Development and validation of a propeller slipstream model for unmanned aerial vehicles," *J. Aircr.*, vol. 52, no. 6, pp. 1985–1994, Jan. 2015.

[13] E. Lavretsky and K. A. Wise, "State feedback direct model reference adaptive control," in *Robust and Adaptive Control*. London, U.K.: Springer, 2013, pp. 40–270.

[14] E. Kharisov, N. Hovakimyan, and K. Åström, "Comparison of several adaptive controllers according to their robustness metrics," in *Proc. AIAA Guid., Navigat., Control Conf.*, 2010, p. 8047.

[15] C. Cao, V. V. Patel, K. Reddy, N. Hovakimyan, E. Lavretsky, and K. Wise, "Are phase and time-delay margins always adversely affected by high-gain," in *Proc. AIAA Guid., Navigat., Control Conf. Exhib.*, 2006, p. 6347.

[16] C. Cao and N. Hovakimyan, "Design and analysis of a novel L_1 adaptive controller, part I: Control signal and asymptotic stability," in *Proc. Amer. Control Conf.*, Minnesota, MN, USA, Jun. 2006, pp. 3397–3402.

[17] C. Cao and N. Hovakimyan, "Design and analysis of a novel L_1 adaptive controller, part II: guaranteed transient performance," in *Proc. Amer. Control Conf.*, Minnesota, MN, USA, Jun. 2006, pp. 3403–3408.

[18] N. Hovakimyan and C. Cao, "State feedback in the presence of matched uncertainties," in L_1 *Adaptive Control Theory: Guaranteed Robustness With Fast Adaptation*, 1st ed. Philadelphia, PA, USA: SIAM, 2010, pp. 17–50.

[19] N. Hovakimyan, C. Cao, E. Kharisov, E. Xargay, and I. M. Gregory, "L₁ adaptive control for safety-critical systems," *IEEE Control Syst. Mag.*, vol. 31, no. 5, pp. 54–104, Oct. 2011.

[20] I. Gregory, C. Cao, V. Patel, and N. Hovakimyan, "Adaptive control laws for flexible semi-span wind tunnel model of high-aspect ratio flying wing," in *Proc. AIAA Guid., Navigat., Control Conf. Exhib.*, Aug. 2007, p. 6625.

[21] I. Gregory, C. Cao, E. Xargay, N. Hovakimyan, and X. Zou, "L₁ adaptive control design for NASA AirSTAR flight test vehicle," in *Proc. AIAA Guid., Navigat., Control Conf.*, Aug. 2009, p. 5738.

[22] R. Hindman, C. Cao, and N. Hovakimyan, "Designing a high performance, stable L1 adaptive output feedback controller," in *Proc. AIAA Guid., Navigat., Control Conf. Exhib.*, 2007, p. 6644.

[23] P. D. Monte and B. Lohmann, "Position trajectory tracking of a quadrotor helicopter based on L_1 adaptive control," in *Proc. Eur. Control Conf. (ECC)*, Jul. 2013, pp. 3346–3353.

[24] I. M. Gregory, F. Xargay, C. Cao, and N. Hovakimyan, "Flight test of L_1 adaptive control law: Offset landings and large flight envelope modeling work," in *Proc. AIAA Guid., Navigat., Control Conf.*, Aug. 2011, p. 6608.

[25] S. Banerjee, Z. Wang, B. Baur, F. Holzapfel, J. Che, and C. Cao, "L₁ adaptive control augmentation for the longitudinal dynamics of a hypersonic glider," *J. Guid., Control, Dyn.*, vol. 39, no. 2, pp. 275–291, Sep. 2015.

[26] E. Capello, G. Guglieri, F. Quagliotti, and D. Sartori, "Design and validation of an L_1 adaptive controller for mini-UAV autopilot," *J. Intell. Robot. Syst.*, vol. 69, nos. 1–4, pp. 109–118, Jan. 2013.

[27] D. Li, N. Hovakimyan, and C. Cao, "L_1 adaptive controller in the presence of input saturation," in *Proc. AIAA Guid., Navigat., Control Conf.*, Aug. 2009, p. 6064.

[28] D. Li, N. Hovakimyan, and C. Cao, "Positive invariant set estimation of L_1 adaptive controller in the presence of input saturation," *Int. J. Adapt. Control Signal Process.*, vol. 27, no. 11, pp. 1012–1030, Nov. 2013.

[29] D. Li, N. Hovakimyan, and C. Cao, "Positive invariance set of L_1 adaptive controller in the presence of input saturation," in *Proc. AIAA Guid., Navigat., Control Conf.*, 2010, p. 7535.

[30] J. Vanness, E. Kharisov, and N. Hovakimyan, "L₁ adaptive control with proportional adaptation law," in *Proc. Amer. Control Conf.*, Montreal, QC, Canada, Jun. 2012, pp. 1919–1924.

[31] K. J. Astrom and L. Rundqwist, "Integrator windup and how to avoid it," in *Proc. Amer. Control Conf.*, Pittsburgh, PA, USA, Jun. 1989, pp. 1693–1698.

[32] (2019). *TBS Caipirinha*. [Online]. Available: https://www.getfpv.com/tbs-caipirinha-fpv-flying-wing.html

[33] (2019). *TBS Caipiroshka*. [Online]. Available: https://docs.px4.io/en/frames_ vtol/vtol_tailsitter_caipiroshka_pixracer.html

[34] J. Zhong, B. Song, W. Yang, and P. Nian, "Modeling and hover control of a dual-rotor tail-sitter unmanned aircraft," in *Proc. Int. Conf. Intell. Robot. Appl.*, Aug. 2017, pp. 589–601.

[35] J. P. How, E. Frazzoli, and G. V. Chowdhary, "Linear flight control techniques for unmanned aerial vehicles," in *Proc. Handbook Unmanned Aerial Vehicles*, 2015, pp. 560–562.

[36] L. Meier, D. Honegger, and M. Pollefeys, "PX4: A node-based multithreaded open source robotics framework for deeply embedded platforms," in *Proc. IEEE Int. Conf. Robot. Autom. (ICRA)*, Seattle, WA, USA, May 2015, pp. 6235–6240.
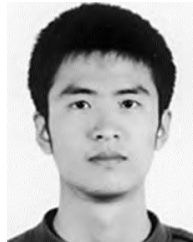
JINGYANG ZHONG received the B.E. degree in aircraft design from Northwestern Polytechnical University, China, in 2013, where he is currently pursuing the Ph.D. degree with the School of Aviation. His research interests include flight control for tail-sitter UAVs and dynamic modeling.

BIFENG SONG received the Ph.D. degree. He was a Distinguished Professor as "Chang Jiang Scholars Program" of Ministry of Education in Aircraft Design Disciplines, 973 Project's Chief Scientist, a Professor, and a Doctoral Supervisor. His current research interests include aircraft multidisciplinary design optimization and the top decision-making technology, design of micro aircraft design, airship design, high survivability technologies and reliability, maintainability, and supportability project.

YUBIN LI received the B.E. and Ph.D. degrees in fluid mechanics from Northwestern Polytechnical University, Xi'an, China, in 1987 and 2000, respectively, where he is currently an Associate Professor with the School of Aviation. His research interests include computational fluid mechanics and control.

JIANLIN XUAN received the B.E. and master's degrees in flight vehicle design engineering from Northwestern Polytechnical University, Xi'an, China, in 2004 and 2007, respectively, where he is currently pursuing the Ph.D. degree in flight vehicle design. He has been teaching with the School of Aviation, Northwestern Polytechnical University, since 2007. His current research interests include the control of flight vehicle system and its application in the industrial process, the influence for flight vehicle from complex environment, the load simulation for flight vehicle, and energy saving control in flight systems.

● ● ●